

Contents

| | | |
|----|--|-----------|
| | S1 Parameterizing the impact of aircraft size on contrail climate effect | 2 |
| | S2 Multiple Regression formulas | 4 |
| | S2.1 Derivation of fuel and NO _x functions | 4 |
| 5 | S2.2 Derivation of climate effect regression functions | 6 |
| | S2.3 Smoothing of Multiple Regression formulas at the cluster boundaries | 11 |
| | S3 Symbolic Regression formulas | 13 |
| | S3.1 Derivation of Symbolic Regression formulas | 13 |
| | S3.2 Smoothing of Symbolic Regression formulas at the cluster boundary | 18 |
| 10 | S4 Climate effect allocation per passenger | 19 |
| | S5 Atmospheric uncertainty estimate | 20 |
| | S6 Comparison to the model from Dahlmann et al. (2023) | 21 |
| | S7 User guide | 24 |

S1 Parameterizing the impact of aircraft size on contrail climate effect

15 The response model AirClim considers the formation of contrails, their coverage and radiative forcing. However, the influence of aircraft size on the contrail climate effect is not regarded specifically. To account for that, a parametrization is derived from a limited set of high-resolution contrail-cirrus simulations of Unterstrasser and Görsch (2014). The parametrization describes the dependency of the climate effect of contrails on the aircraft size using the wing span b as proxy (Fig. S1 left).

The wing span, aircraft mass and fuel consumption depend on the aircraft type; Unterstrasser and Görsch (2014) studied 20 contrails from different aircraft types ranging from a CRJ regional airliner ($b = 21$ m) to an Airbus A380 ($b = 80$ m). For a given soot emission index, a higher fuel consumption implies a larger number of ice crystals in the contrail. Moreover, larger and heavier aircraft induce stronger wake vortices, which descend further down and increase the contrail dimensions after the vortex phase (spanning the first few minutes). Both aspects (change of early ice crystal number and contrail dimensions) have been shown to have a long-lasting impact on the properties of the evolving contrail-cirrus.

25 For the present study, the total extinction time series, as shown in Fig. 9 of Unterstrasser and Görsch (2014), is integrated over time to obtain a single-value proxy for the radiative impact of the contrail-cirrus over their full life cycle (the integration procedure is motivated in Sec 3.3 of Unterstrasser, 2020). The left plot shows the time-integrated total extinction \tilde{E} as a function of aircraft size for three different atmospheric scenarios. Clearly, \tilde{E} increases with b and depends on the atmospheric

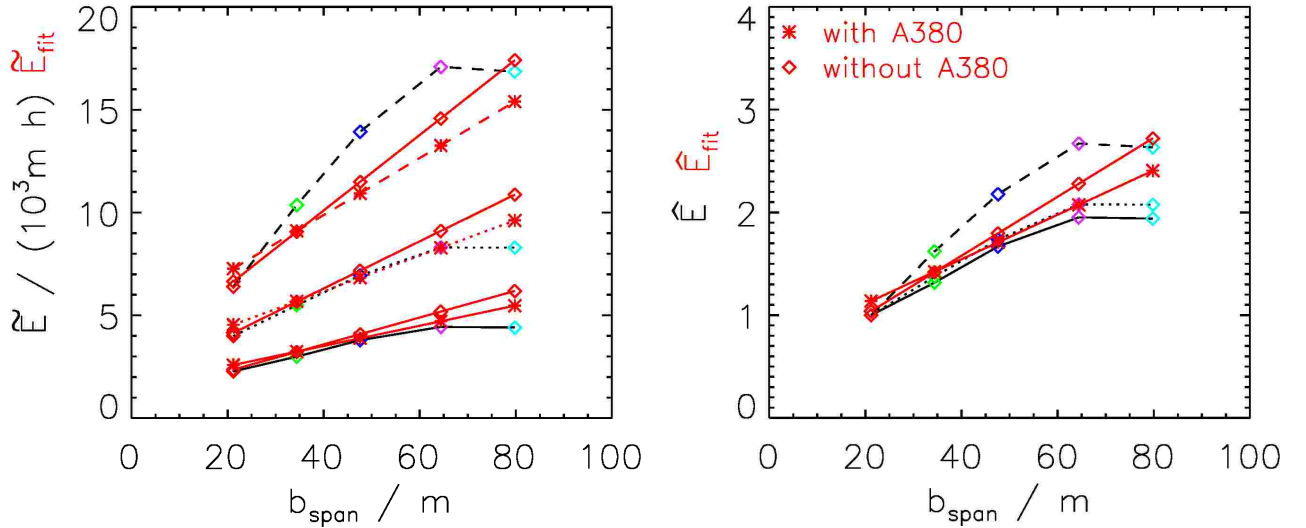


Figure S1. Correlation between wingspan (as an indicator for the aircraft size) and time-integrated total extinction (left) and normalized time-integrated total extinction (right). The latter quantity uses the extinction value of $b = 20\text{m}$ for normalization. Three different environmental conditions for atmospheric updraft and wind shear (symbols) are considered for 5 aircraft types (color). The red lines show linear correlations with (star) and without (diamond) considering the Airbus A380 aircraft data points.

scenario. As a next step, \tilde{E} is normalized by the \tilde{E} value of the CRJ aircraft. Hence, all curves in the right panel start at $\hat{E} = 1$ for $b = 21$ m. It can be seen that the relative increase of \hat{E} is fairly similar across the three atmospheric scenarios. Previous radiative transfer calculations showed that relative changes in total extinction translate into similar relative changes of the contrail radiative effect (for fixed atmospheric scenarios). A linear fit (red lines in the right panel), approximating the \hat{E} data points as a function of b , enables us to account for the aircraft size in the contrail RF computation in AirClim. The relative change between two aircraft (AC1, AC2) is given by

$$\frac{\hat{E}_{AC1}}{\hat{E}_{AC2}} = \frac{v + w \times b_{AC1}}{v + w \times b_{AC2}}, \text{ where } v = 0.43 \text{ and } w = 0.0287 \text{ m}^{-1}. \quad (\text{Eq. S1})$$

Using as a reference a wing span of 38 m, we obtain an adaptation factor for the contrail climate effect due to different aircraft sizes of

$$f_{ACsize}(b) = \frac{v + w \times b}{v + w \times b_{ref}}, \text{ where } b \in [20 \text{ m}, 80 \text{ m}] \text{ and } b_{ref} = 38 \text{ m}. \quad (\text{Eq. S2})$$

The simulation data base of Unterstrasser and Görsch (2014) includes only simulations, where all aircraft-dependent parameters like wing span b , fuel consumption m_C and aircraft mass m_{AC} are changed simultaneously (see Table 1 in Unterstrasser and Görsch (2014)). Therefore, the correction cannot be employed to estimate how the contrail effect changes with wing span for fixed aircraft mass or fuel consumption. Moreover, a soot emission index of 2.8×10^{14} is used. Hence, the correction formula is only valid for aircraft with conventional design and kerosene combustion with present-day soot emission index. The correction should only be applied for values of m_C and m_{AC} in the ranges given by:

$$m_C / \left(\frac{\text{kg}}{\text{km}} \right) = \left(\frac{b}{18.23 \text{ m}} \right)^{1.87} \times 1.2^x \quad (\text{Eq. S3})$$

$$m_{AC} / \text{tons} = \left(\frac{b}{6.11 \text{ m}} \right)^{2.4} \times 1.2^x \quad (\text{Eq. S4})$$

The variable x runs from -1 to 1 and characterizes a 20% margin around the nominal values.

In Unterstrasser and Görsch (2014), the aim was to demonstrate the long-lasting impact of the aircraft type on contrail-cirrus properties. However, no systematic survey was performed at that time and the data set is limited in the sense that only three different synoptic scenarios have been analyzed. Hence, the correction formula should only be interpreted and employed as a rough first-order estimate of the influence of the size of conventional aircraft on contrail radiative properties.

While the derived parametrization is already included in the ATR100 climate effect values for contrails used for the SR-approach, the climate effect of contrails calculated with the MR-formulas has to be scaled during post-processing by the factor f_{ACsize} , which requires the wingspan b as an additional input parameter.

55 S2 Multiple Regression formulas

The following section outlines the development of Multiple Regression formulas. The estimation of the total ATR100 is based on regression formulas for fuel and NO_x emissions as well as climate effect functions, that are combined according to the following structure across all clusters:

$$\text{ATR100}_{\text{tot}} = c_{\text{CO}_2} \cdot f + c_{\text{NO}_x}(d, \bar{\phi}) \cdot e + c_{\text{H}_2\text{O}}(d, \bar{\phi}) \cdot f + c_{\text{C}_2\text{F}_6}(d, \bar{\phi}) \cdot d \cdot f_{\text{ACsize}}(b) \quad (\text{Eq. S5})$$

60 Section S2.1 derives fuel and NO_x functions used for f and e , if they are unknown. The amount of NO_x e is not regressed directly, but the emission index EI_{NO_x} which is defined as mass of emitted NO_x per mass of consumed fuel. In Section S2.2 the derivation of climate effect functions (c_x) follows and we conclude with the smoothing of MR formulas in Section S2.3.

S2.1 Derivation of fuel and NO_x functions

Using a selection of all flights of a given seat category from the database, we derived regression formulas which approximate the
 65 burned fuel f and the NO_x emission index (EI_{NO_x}) for a given flight distance d (Fig. S2). These regression formulas are based on fuel uses and NO_x emission indices derived from the Boeing and DLR fuel flow methods. Note, that for the derivation of the

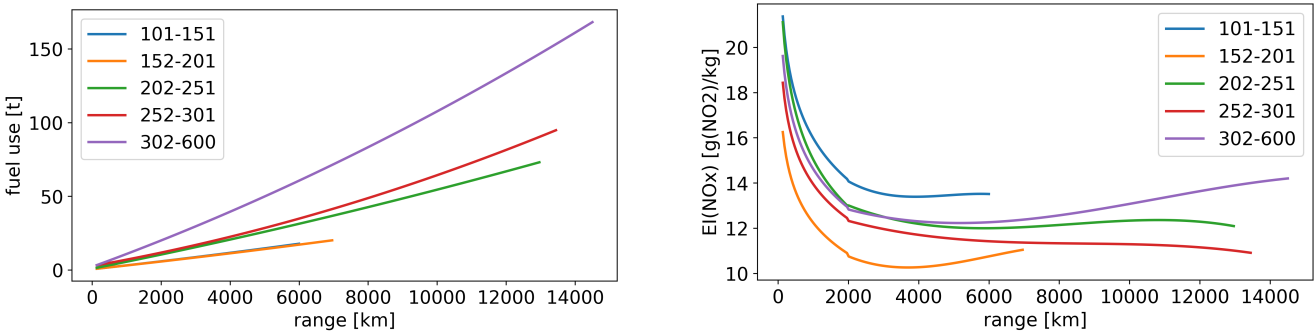


Figure S2. Fuel functions for the simplified calculation of burnt fuel (left) and NO_x functions for the simplified calculation of the NO_x emission index (right) both as a function of flight distance.

Table S1. Best fit solutions for fuel Multiple Regression formulas.

| Seat category | maximum range [km] | a_0 [kg] | a_1 [kg km ⁻¹] | a_2 [kg km ⁻²] | R^2 |
|---------------|--------------------|------------|------------------------------|------------------------------|--------|
| 101-151 | 6,000 | 632.36 | 2.5809 | 5.0×10^{-5} | 0.9997 |
| 152-201 | 7,000 | 629.27 | 2.5388 | 3.8×10^{-5} | 0.9992 |
| 202-251 | 13,000 | 997.62 | 4.6586 | 7.3×10^{-5} | 0.9994 |
| 252-301 | 13,450 | 2,789.10 | 4.1618 | 2.2×10^{-4} | 0.9907 |
| 302-600 | 14,500 | 2,277.30 | 8.5406 | 2.4×10^{-4} | 0.9999 |

Table S2. Best fit solutions for EI_{NO_x} Multiple Regression formulas for flight distances < 2000km.

| Seat category | b_0 [g(NO ₂) kg ⁻¹] | b_1 [g(NO ₂) kg ⁻¹] | R^2 |
|---------------|---|---|-------|
| 101-151 | 34.403 | -2.667 | 0.868 |
| 152-201 | 25.963 | -1.986 | 0.892 |
| 202-251 | 35.811 | -3.007 | 0.923 |
| 252-301 | 29.287 | -2.220 | 0.930 |
| 302-600 | 31.717 | -2.475 | 0.971 |

Table S3. Best fit solutions for EI_{NO_x} Multiple Regression formulas for flight distances ≥ 2000km.

| Seat category | b_2 [g(NO ₂) kg ⁻¹] | b_3 [g(NO ₂) kg ⁻¹ km ⁻¹] | b_4 [g(NO ₂) kg ⁻¹ km ⁻²] | b_5 [g(NO ₂) kg ⁻¹ km ⁻³] | R^2 |
|---------------|---|--|--|--|-------|
| 101-151 | 17.478 | -2.70×10^{-3} | 5.8×10^{-7} | -4×10^{-11} | 0.978 |
| 152-201 | 13.163 | -1.84×10^{-3} | 3.6×10^{-7} | -2×10^{-11} | 0.992 |
| 202-251 | 14.742 | -1.14×10^{-3} | 1.5×10^{-7} | -6×10^{-12} | 0.970 |
| 252-301 | 13.428 | -6.93×10^{-4} | 7.8×10^{-8} | -3×10^{-12} | 0.970 |
| 302-600 | 13.992 | -7.61×10^{-4} | 9.7×10^{-8} | -3×10^{-12} | 0.970 |

climate effect regression formulas, the exact values for each flight are used and not the fuel and NO_x functions derived here. Nonetheless, we provide them as additional information that might be useful and can be applied in the simplified estimation of a flight's climate effect, as only the seat category and the flight distance are required for their computation. Fuel functions

obey the pattern

$$f = a_0 + a_1 d + a_2 d^2, \quad (\text{Eq. S6})$$

with the coefficients a_i as given in Table S1. The coefficient of determination R^2 is > 0.99 for all seat categories.

The derived EI_{NO_x} regression formulas vary for distances smaller and larger than 2000 km and are described by

$$\text{EI}_{\text{NO}_x} = \begin{cases} b_0 + b_1 \ln \frac{d}{\text{km}} & \text{if } d < 2000 \text{ km} \\ b_2 + b_3 d + b_4 d^2 + b_5 d^3 & \text{if } d \geq 2000 \text{ km}. \end{cases} \quad (\text{Eq. S7})$$

Best fit solutions for EI_{NO_x} regression formulas are provided in Tables S2 and S3 and Figure S2.

An interesting feature of the NO_x functions (Eq. S7; Fig. S2) is the lack of correlation between the seat category and the EI_{NO_x}. The EI_{NO_x} mainly depends on the combustion temperature, with a higher temperature leading to more emissions. The combustion temperature depends on the properties of the engine in the specific aircraft. For the computation of the NO_x functions, aircraft that are frequently used within their seat category were chosen, but these are not necessarily representative of the entirety of used aircraft within that seat category. In particular, the most efficient and therefore economically successful aircraft may be overrepresented.

S2.2 Derivation of climate effect regression functions

Figures S3-S6 show the climate effect of each flight as functions of the flight distance and the mean latitude for the different clusters. Due to the lower background concentrations in the southern hemisphere, NO_x emissions there have a stronger climate effect than in the northern hemisphere (Fig. S4b; Fig. S5b) (Köhler et al., 2013). The climate effect of H_2O is largest when it is emitted in the lower stratosphere. Therefore, it is low in the tropics (Fig. S5e), where the tropopause lies above cruise altitude. The same accounts for short flights at any latitude (Fig. S3d), as these do not reach the stratosphere. Similarly, very short flights often do not reach the required altitude for contrail formation (Fig. S3g). The contrail–cirrus climate effect is largest for flights in the tropics (Fig. S5h) due to the increased radiation. The usage of clusters enables us to find climate effect regression functions that closely align with these patterns.

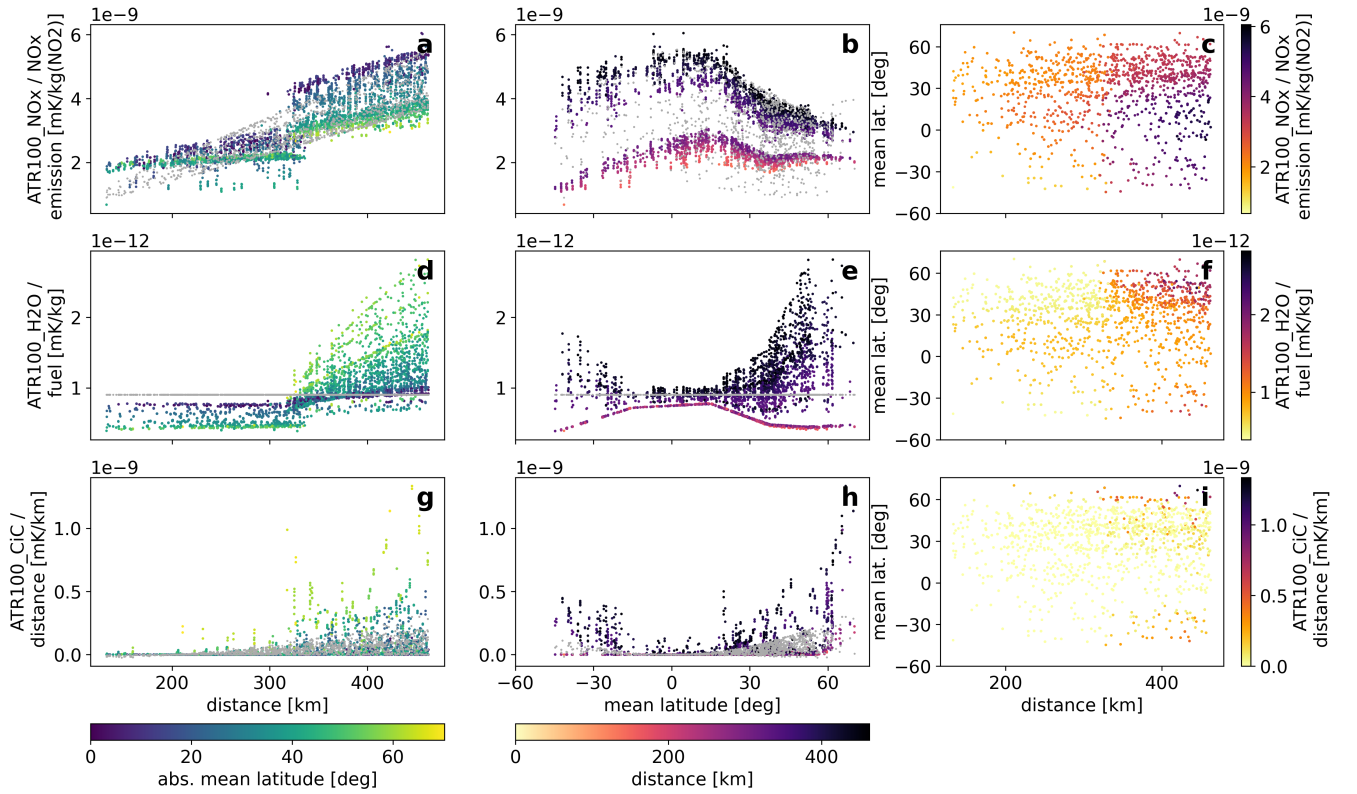


Figure S3. Climate metrics $\text{ATR100}_{\text{NO}_x}/e$ (top row), $\text{ATR100}_{\text{H}_2\text{O}}/f$ (middle row), $\text{ATR100}_{\text{CiC}}/d$ (bottom row) as a function of distance d (left column), mean latitude $\bar{\phi}$ (middle column), and both (right column) for the short-flight cluster. Colored dots denote the values obtained from AirClim and gray dots are fit results from the climate effect functions (Eq. S8- Eq. S19).

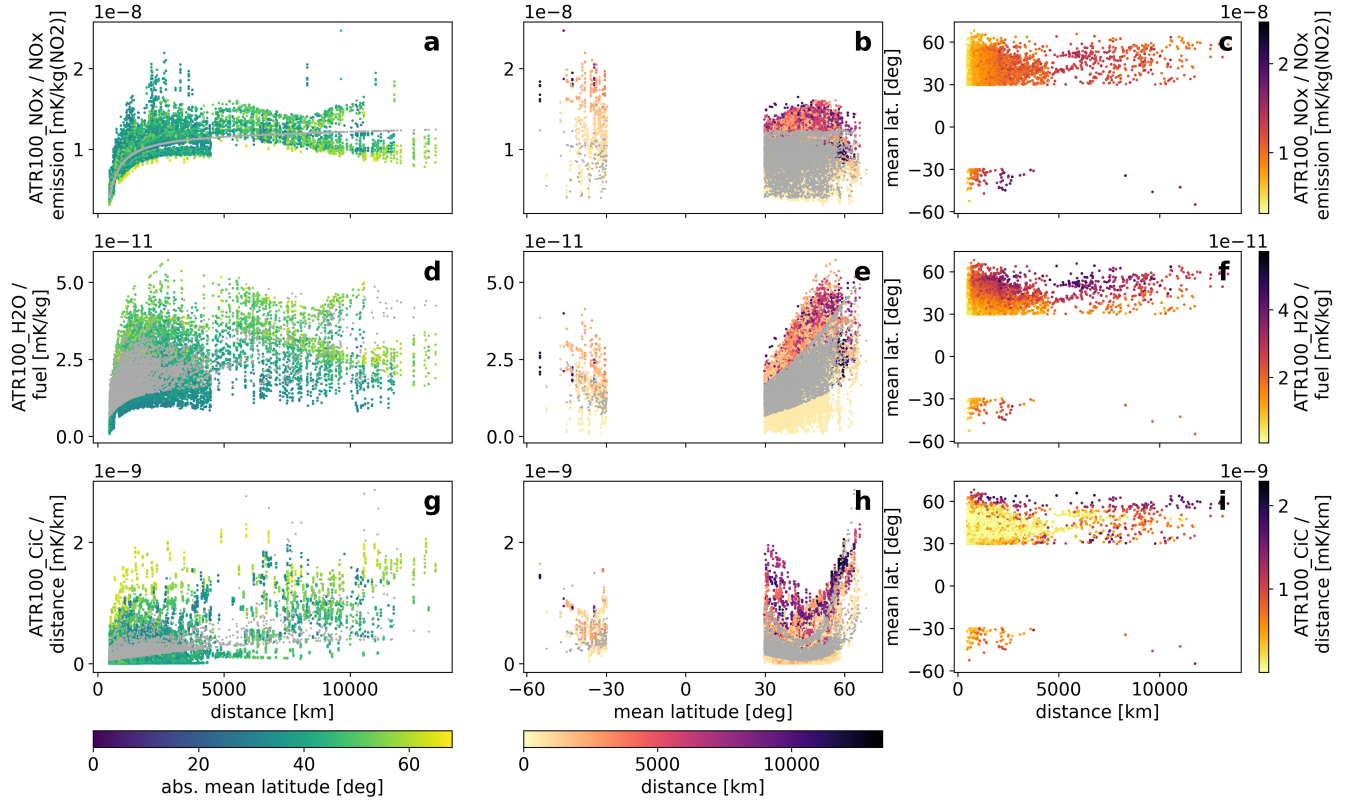


Figure S4. Same as Figure S3, but for the mid-latitude cluster.

The partial cluster-dependent climate effect functions are chosen based on the behavior of the respective values in latitude–distance space (Fig. S3 - Fig. S5) as

$$c_{\text{NO}_x, \text{short}} = (a_{\text{NO}_x, s, 0}d + a_{\text{NO}_x, s, 1}) \times (a_{\text{NO}_x, s, 2}\bar{\phi}^4 + a_{\text{NO}_x, s, 3}\bar{\phi}^3 + a_{\text{NO}_x, s, 4}\bar{\phi}^2 + a_{\text{NO}_x, s, 5}\bar{\phi} + a_{\text{NO}_x, s, 6}) \quad (\text{Eq. S8})$$

$$c_{\text{H}_2\text{O}, \text{short}} = a_{\text{H}_2\text{O}, s, 0} \quad (\text{Eq. S9})$$

$$95 \quad c_{\text{CiC}, \text{short}} = \max(0, (a_{\text{CiC}, s, 0}d^2 + a_{\text{CiC}, s, 1}d + a_{\text{CiC}, s, 2})\bar{\phi}^2) \quad (\text{Eq. S10})$$

for the short-flight cluster,

$$c_{\text{NO}_x, \text{mid-latitude}} = a_{\text{NO}_x, m, 0} \arctan(a_{\text{NO}_x, m, 1}d) + a_{\text{NO}_x, m, 2}d + a_{\text{NO}_x, m, 3} \quad (\text{Eq. S11})$$

$$c_{\text{H}_2\text{O}, \text{mid-latitude}} = a_{\text{H}_2\text{O}, m, 0} \arctan(a_{\text{H}_2\text{O}, m, 1}d) \times (a_{\text{H}_2\text{O}, m, 2}\bar{\phi}^2 + a_{\text{H}_2\text{O}, m, 3}) \quad (\text{Eq. S12})$$

$$100 \quad c_{\text{CiC}, \text{mid-latitude}} = \max(0, (a_{\text{CiC}, m, 0}d^2 + a_{\text{CiC}, m, 1}d + a_{\text{CiC}, m, 2}) \times (a_{\text{CiC}, m, 3}\bar{\phi}^4 + a_{\text{CiC}, m, 4}\bar{\phi}^3 + a_{\text{CiC}, m, 5}\bar{\phi}^2 + a_{\text{CiC}, m, 6}\bar{\phi} + a_{\text{CiC}, m, 7})) \quad (\text{Eq. S13})$$

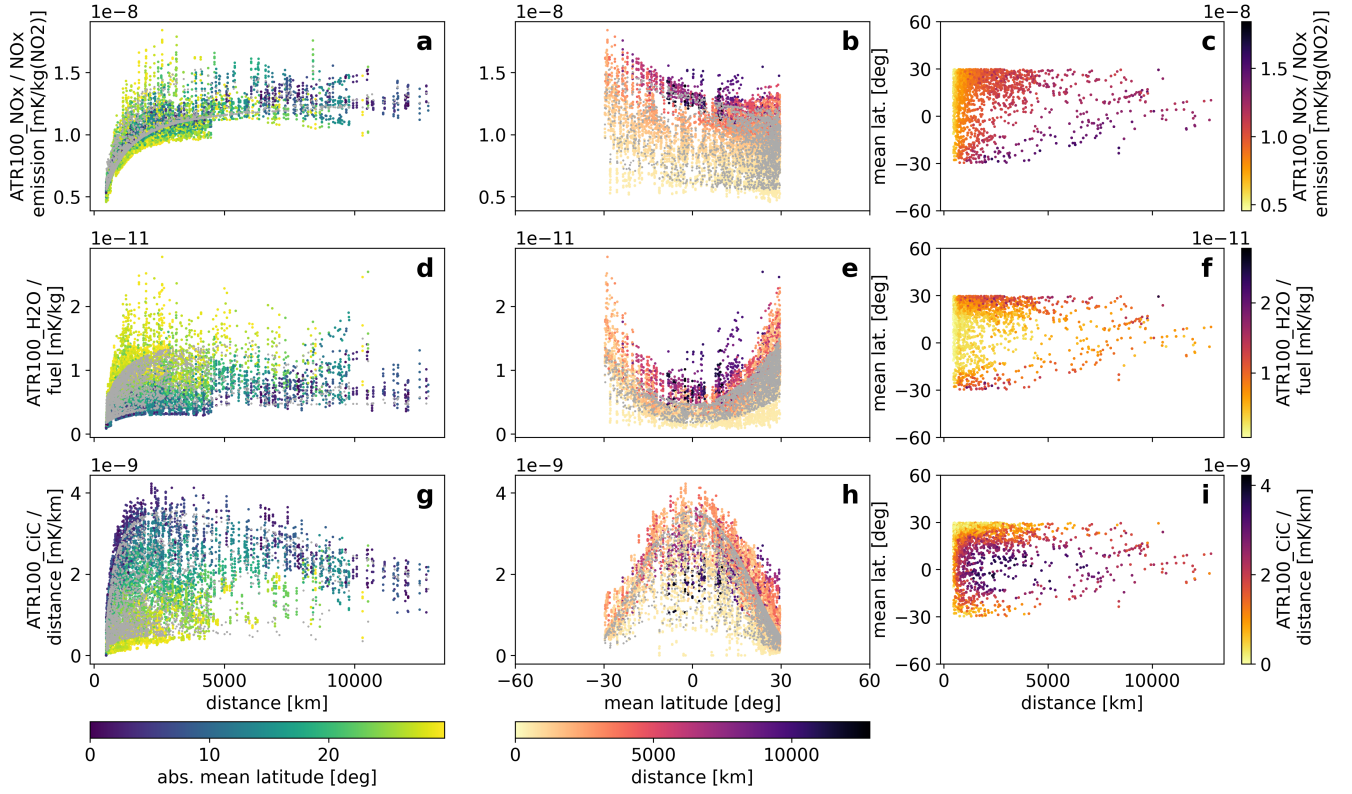


Figure S5. Same as Figure S3, but for the tropical cluster.

for the mid-latitude cluster,

$$c_{\text{NO}_x, \text{tropical}} = (a_{\text{NO}_x, t, 0} \arctan(a_{\text{NO}_x, t, 1} d) + a_{\text{NO}_x, t, 2}) \times (a_{\text{NO}_x, t, 3} \bar{\phi}^2 + a_{\text{NO}_x, t, 4} \bar{\phi} + a_{\text{NO}_x, t, 5}) \quad (\text{Eq. S14})$$

$$c_{\text{H}_2\text{O}, \text{tropical}} = a_{\text{H}_2\text{O}, t, 0} \arctan(a_{\text{H}_2\text{O}, t, 1} d) \times (a_{\text{H}_2\text{O}, t, 2} \bar{\phi}^2 + a_{\text{H}_2\text{O}, t, 3}) \quad (\text{Eq. S15})$$

$$c_{\text{CiC}, \text{tropical}} = \max(0, (a_{\text{CiC}, t, 0} \arctan(a_{\text{CiC}, t, 1} d) + a_{\text{CiC}, t, 2} d + a_{\text{CiC}, t, 3}) \times (a_{\text{CiC}, t, 4} \bar{\phi}^4 + a_{\text{CiC}, t, 5} \bar{\phi}^2 + a_{\text{CiC}, t, 6})) \quad (\text{Eq. S16})$$

105 for the tropical cluster, and

$$c_{\text{NO}_x, \text{regional}} = a_{\text{NO}_x, r, 0} + a_{\text{NO}_x, r, 1} d + a_{\text{NO}_x, r, 2} d^2 \quad (\text{Eq. S17})$$

$$c_{\text{H}_2\text{O}, \text{regional}} = \max(0, (a_{\text{H}_2\text{O}, r, 0} + a_{\text{H}_2\text{O}, r, 1} d + a_{\text{H}_2\text{O}, r, 2} d^2 + a_{\text{H}_2\text{O}, r, 3} d^3) \times (1 + a_{\text{H}_2\text{O}, r, 4} \times \bar{\phi}^2)) \quad (\text{Eq. S18})$$

$$c_{\text{CiC}, \text{regional}} = \max(0, (a_{\text{CiC}, r, 0} + a_{\text{CiC}, r, 1} d + a_{\text{CiC}, r, 2} d^2) \times (1 + a_{\text{CiC}, r, 3} \bar{\phi}^2 + a_{\text{CiC}, r, 4} \bar{\phi}^4 + a_{\text{CiC}, r, 5} \bar{\phi}^6)) \quad (\text{Eq. S19})$$

for the regional cluster.

110 The inputs for these climate effect functions are the flight distance d in km and the mean latitude $\bar{\phi}$ in degrees. The resulting climate effects are given in units of $\text{mKkg}^{-1}(\text{NO}_2)$ for c_{NO_x} , $\text{mKkg}^{-1}(\text{fuel})$ for $c_{\text{H}_2\text{O}}$, and mKkm^{-1} for c_{CiC} , respectively. The climate effects, particularly those of NO_x and H_2O , exhibit discontinuities at flight distances of ≈ 315 km and

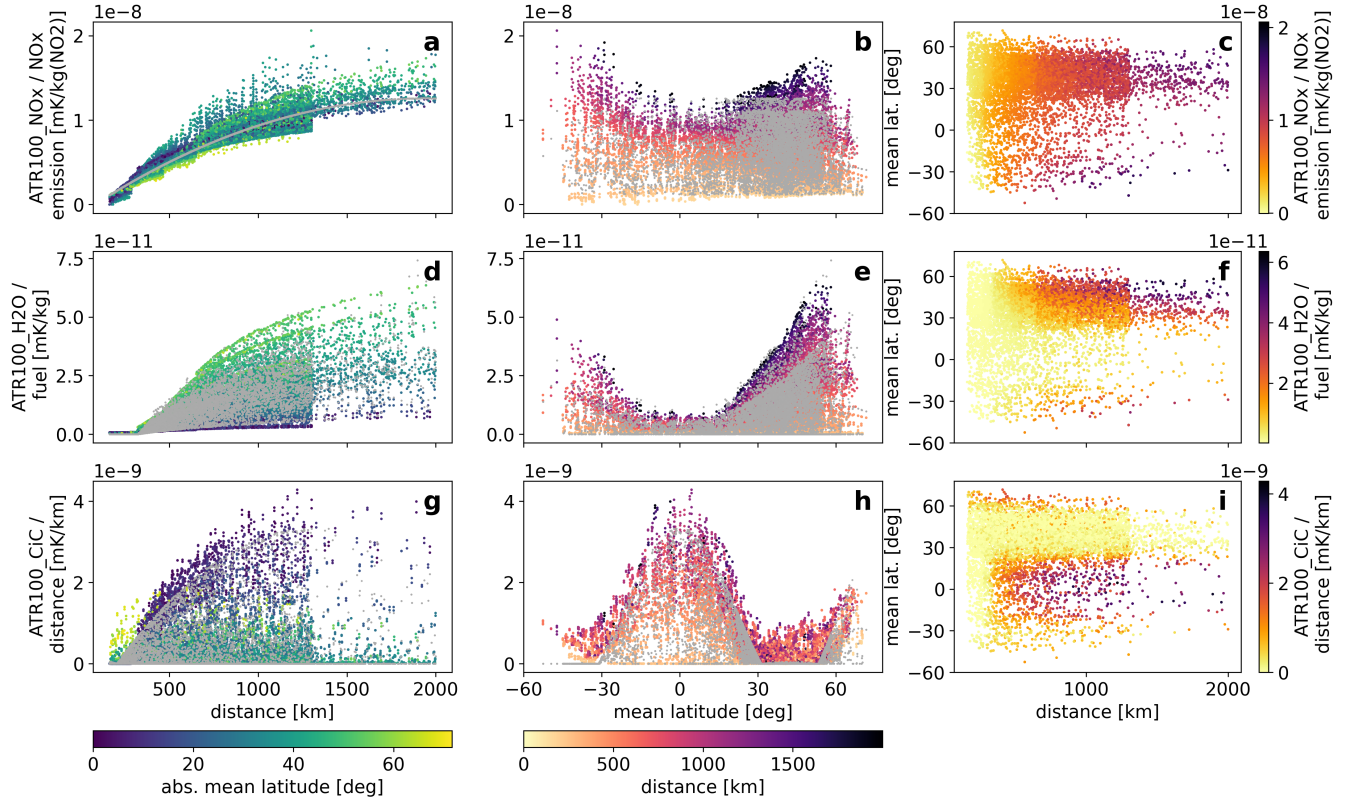


Figure S6. Same as Figure S3, but for the regional cluster.

≈ 4600 km, which are related to higher calculated flight levels for flights with longer distances. These discontinuities pose challenges on the fitting with continuous analytic functions. In the case of the H₂O climate effect for the short-flight cluster, we chose to use the mean value instead of a more sophisticated formula, as the contribution of H₂O to the total climate effect is very low for short flights in any case. The latitudinal dependency of the climate effects is generally modelled with polynomials, where the number of terms depends on the complexity and symmetry of the data's behavior. The dependency of the climate effects on the flight distance is modelled using a combination of polynomial terms and arctangents, which capture the behavior of an initial steep increase in and later flattening of the climate effect data (see also Dahlmann et al., 2023). The coefficients a_i are determined for each of the nine MR-formulas by a non-linear least-squares fit and are given in Table S4.

Table S4: Best-fit solutions for the coefficients in Eq. S8-Eq. S19. These coefficients are only valid when using the respective equations with flight distances d in km and mean latitudes $\bar{\phi}$ in degrees.

| short-flight cluster | | | |
|----------------------|--------------------------------|---------------------------------------|-------------------------------|
| i | $a_{\text{NO}_x, \text{r}, i}$ | $a_{\text{H}_2\text{O}, \text{r}, i}$ | $a_{\text{CiC}, \text{r}, i}$ |
| 0 | $2.00347786 \times 10^{-15}$ | $9.03099431 \times 10^{-13}$ | $4.56196374 \times 10^{-19}$ |
| 1 | $-7.13997187 \times 10^{-14}$ | — | $-1.95682151 \times 10^{-17}$ |
| 2 | 2.365071×10^{-4} | — | $-1.4614218 \times 10^{-14}$ |
| 3 | $1.54249099 \times 10^{-4}$ | — | — |
| 4 | -1.4608542 | — | — |
| 5 | 1.1732398 | — | — |
| 6 | 6.47293618×10^3 | — | — |
| mid-latitude cluster | | | |
| i | $a_{\text{NO}_x, \text{m}, i}$ | $a_{\text{H}_2\text{O}, \text{m}, i}$ | $a_{\text{CiC}, \text{m}, i}$ |
| 0 | $4.78782759 \times 10^{-4}$ | $1.11758077 \times 10^{-12}$ | $2.56886171 \times 10^{-21}$ |
| 1 | 1.28634039×10^2 | 1.4423854×10^{-3} | $-5.84017454 \times 10^{-17}$ |
| 2 | $5.2802694 \times 10^{-14}$ | $5.91431647 \times 10^{-3}$ | $-3.02860089 \times 10^{-14}$ |
| 3 | $-7.52058168 \times 10^{-4}$ | 4.86022794 | $-1.36665996 \times 10^{-3}$ |
| 4 | — | — | $-1.17906742 \times 10^{-2}$ |
| 5 | — | — | 5.452753 |
| 6 | — | — | 5.03288373×10^1 |
| 7 | — | — | -7.7344541×10^3 |
| tropical cluster | | | |
| i | $a_{\text{NO}_x, \text{t}, i}$ | $a_{\text{H}_2\text{O}, \text{t}, i}$ | $a_{\text{CiC}, \text{t}, i}$ |
| 0 | $1.41434794 \times 10^{-1}$ | $1.04883173 \times 10^{-8}$ | $3.58811246 \times 10^{-5}$ |
| 1 | $1.15507399 \times 10^{-3}$ | $1.35263527 \times 10^{-3}$ | 2.18840126×10^1 |
| 2 | 4.9301452×10^{-2} | $7.62155078 \times 10^{-7}$ | $-1.91139484 \times 10^{-13}$ |
| 3 | $6.06235609 \times 10^{-12}$ | $2.94922714 \times 10^{-4}$ | $-5.63576858 \times 10^{-5}$ |
| 4 | $-2.90148707 \times 10^{-10}$ | — | $5.92278899 \times 10^{-7}$ |
| 5 | $5.02677523 \times 10^{-8}$ | — | $-1.63789849 \times 10^{-3}$ |
| 6 | — | — | 1.13661959 |

Continued on next page

| regional cluster | | | |
|------------------|-------------------------------|--------------------------------|-------------------------------|
| i | $a_{\text{NO}_x, r, i}$ | $a_{\text{H}_2\text{O}, r, i}$ | $a_{\text{CiC}, r, i}$ |
| 0 | $-1.09548392 \times 10^{-9}$ | $-4.16502250 \times 10^{-12}$ | $-1,32549723 \times 10^{-9}$ |
| 1 | $1.40726150 \times 10^{-11}$ | $1.59411920 \times 10^{-14}$ | $7,0740753 \times 10^{-12}$ |
| 2 | $-3.62230426 \times 10^{-15}$ | $-1.03721504 \times 10^{-17}$ | $-2,67638388 \times 10^{-15}$ |
| 3 | — | $3.03652652 \times 10^{-21}$ | $-1,52841898 \times 10^{-3}$ |
| 4 | — | $2.02919855 \times 10^{-3}$ | $5,7137359 \times 10^{-7}$ |
| 5 | — | — | $-5,52315388 \times 10^{-11}$ |

S2.3 Smoothing of Multiple Regression formulas at the cluster boundaries

Since the climate effect functions for the different clusters are independent of each other, mismatches at the cluster boundaries cannot be avoided (Fig. S7 - Fig. S8). The lines in Figures S7-S8 indicate the climate effect at the cluster boundary calculated using the equations for either cluster for a flight with average NO_x emissions and fuel use. The difference between lines of the same color indicates the mismatch. For average NO_x emissions and fuel use cases, the maximum mismatch is 83%. Particularly large mismatches are found between the short-flight and the tropical cluster for flights with a mean latitude in the equatorial region (Fig. S8), as well as for very long flights between the mid-latitude and tropical clusters (Fig. S7). We also calculated the climate effect at the cluster boundary using either cluster for flights with minimal and maximal NO_x emissions and for flights with minimal and maximal fuel use and found that the most extreme mismatch, reaching 128%, is between calculations using the climate effect functions for the tropical and mid-latitude cluster for a flight with maximal NO_x emissions at very long flight distances with a mean latitude of 29.7°S .

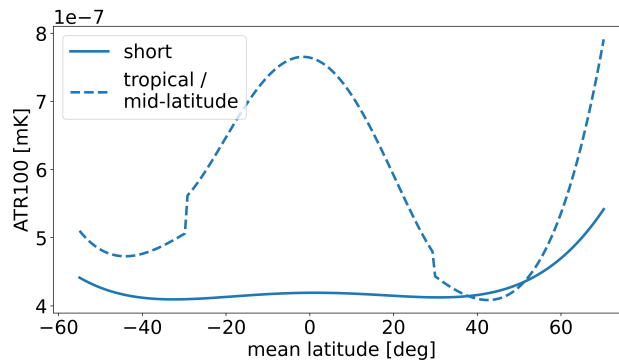


Figure S7. ATR100 at the cluster boundary of 462 km computed from different clusters' climate effect functions for average NO_x emissions and fuel use. Average conditions are taken as the average of all flights with flight distances of $462 \pm 50\text{km}$.

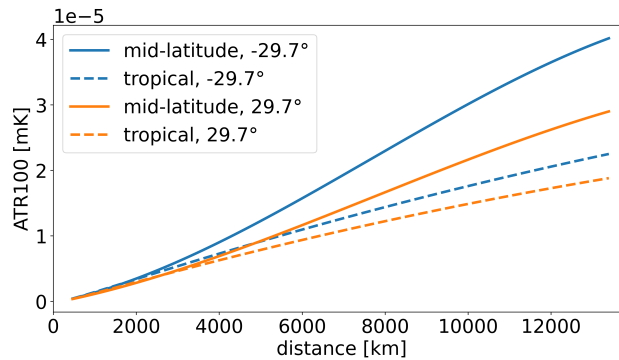


Figure S8. ATR100 at the cluster boundaries of 29.7°N (blue) and 29.7°S (orange) computed from different clusters' climate effect functions. The average fuel use per flight distance and NO_x emissions per flight distance of all flights with mean latitudes of $29.7 \pm 2^\circ$ N and $29.7 \pm 2^\circ$ S, respectively, were used in the computation.

The MR-formulas are divided into four clusters. As the regional cluster is split by seat categories and no numerical parameter its cluster boundaries are not smoothed. Smoothing is applied to the cluster boundary between the tropical and mid-latitude cluster and in a second step to their boundary with the short-flight cluster. The values for the smoothing boundaries are derived
135 R^2 -optimal within preset limits (latitude 5° - 15° and distance minimum 50 km) and are given in Table S5. The quality of estimation slightly decreases in terms of R^2 and slightly increases in terms of MARE through the smoothing (see Tab. S6).

Table S5. Definitions for smoothing of Multiple Regression formulas

| Cluster boundary | Boundary value | Smoothing boundary 1 (b_{C1}) | Smoothing boundary 2 (b_{C2}) |
|-------------------------------|------------------|-----------------------------------|-----------------------------------|
| tropical - mid-latitude | $\pm 29.7^\circ$ | 15° | 5° |
| short - tropical/mid-latitude | 462.5 km | 50 km | 50 km |

Table S6. R^2 and MARE of the unsmoothed and smoothed Multiple Regression formulas.

| | Unsmoothed | Smoothed |
|-------|------------|----------|
| R^2 | 0,9662 | 0,9619 |
| MARE | 21,0 % | 20,7 % |

S3 Symbolic Regression formulas

The second approach to derive climate effect functions from the presented database is the genetic programming approach of Symbolic Regression. It does not require a certain structure of the formula, but evolves it in an evolutionary optimization process. The climate effect of CO₂-, H₂O- and NO_x-emissions as well as contrails in terms of ATR100 is estimated directly without intermediate steps in this approach, to reduce complexity. In Section S3.1 the process of deriving the SR-formulas is described in detail and Section S3.2 specifies the smoothing of the SR-formulas.

S3.1 Derivation of Symbolic Regression formulas

Compared to the MR-approach some changes are applied to the underlying database. Firstly, SR uses the parameter for the mean latitude $\bar{\phi}$ as an unsigned value, while it was signed in the MR-approach. Secondly, to utilize the original three clusters derived using K-means from Section 2.3 and because the so called regional flights do not show an overall distinguishable characteristic in Figure S6, flights of the two smallest aircraft seat categories of 20-50 seats and 51-100 seats are classified into the three clusters according to flight distance and mean latitude. The regional flights were not included in the clustering analysis and are added to the database to expand the potential area of application.

The used SR software, GPTIPS 2, has several hyperparameters to specify the behavior of the program and the properties of the derived formula (Searson, 2015). In a pretest for the present study the goal was to identify the influence of major hyperparameters and to find optimal settings for those by applying the gridsearch method. In a gridsearch every combination of a predefined set of options for selected hyperparameters is executed ones. One result is that for the test most parameters did not have a measurable effect on the quality of the resulting formula at all or if their value is set beyond a certain edge. Parameters with a clear influence are the number and depth of genes. The major result of the pretest is that the random variability of the quality of the resulting formulas measured by the error metric is large. This means, that better individuals can likely be found by running the same optimization several times.

To consider the described variability, a gridsearch approach is chosen to create a large number of almost equally configured runs, while still having different levels of complexity in the derived formulas through different prescribed numbers and depths of genes. The mathematical operations allowed for the formulas are plus, minus, times, times with three factors, divide, root, arctangent, exponential and logarithm. For every run of GPTIPS 2 the resulting best regression formula in terms of R^2 together with its characteristics is saved. This data is used, to find the Pareto-optimal formulas with regard to R^2 and the number of nodes from all runs. In Figure S9 the Pareto-plots for the unclustered version are displayed and in Figure S10 for the clustered version. There is one Pareto-plot for every species.

The quality of a derived formula is evaluated by the number of nodes representing the complexity and the coefficient of determination (R^2) as the error metric representing the estimation quality for the whole dataset. It has to be noted, that due to the saved data from the GPTIPS 2-runs, for the Pareto-plots in Figure S9 and Figure S10, R^2 represents the average of R^2 for the training- and test dataset. The other Pareto-plots show R^2 for the whole dataset. Due to minor differences between R^2 for training- and test dataset (mean difference: 0.2%, max. difference: 3.5%), this is evaluated acceptable.

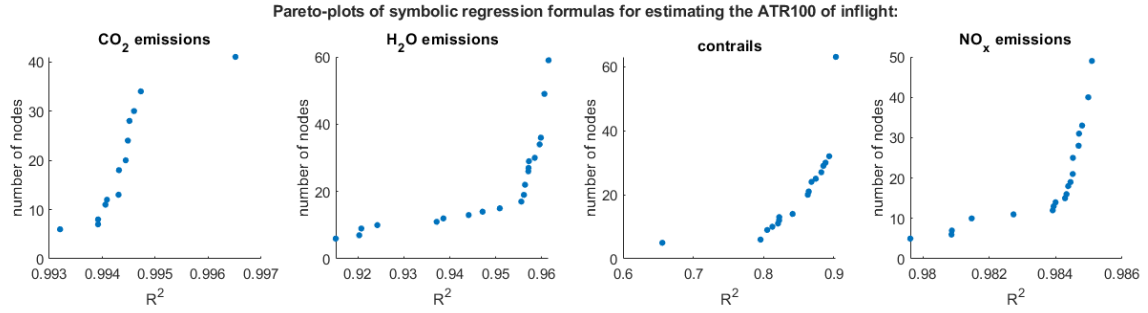


Figure S9. Pareto plots for the derived climate effect formulas from the unclustered gridsearch for CO₂ and non-CO₂ effects.

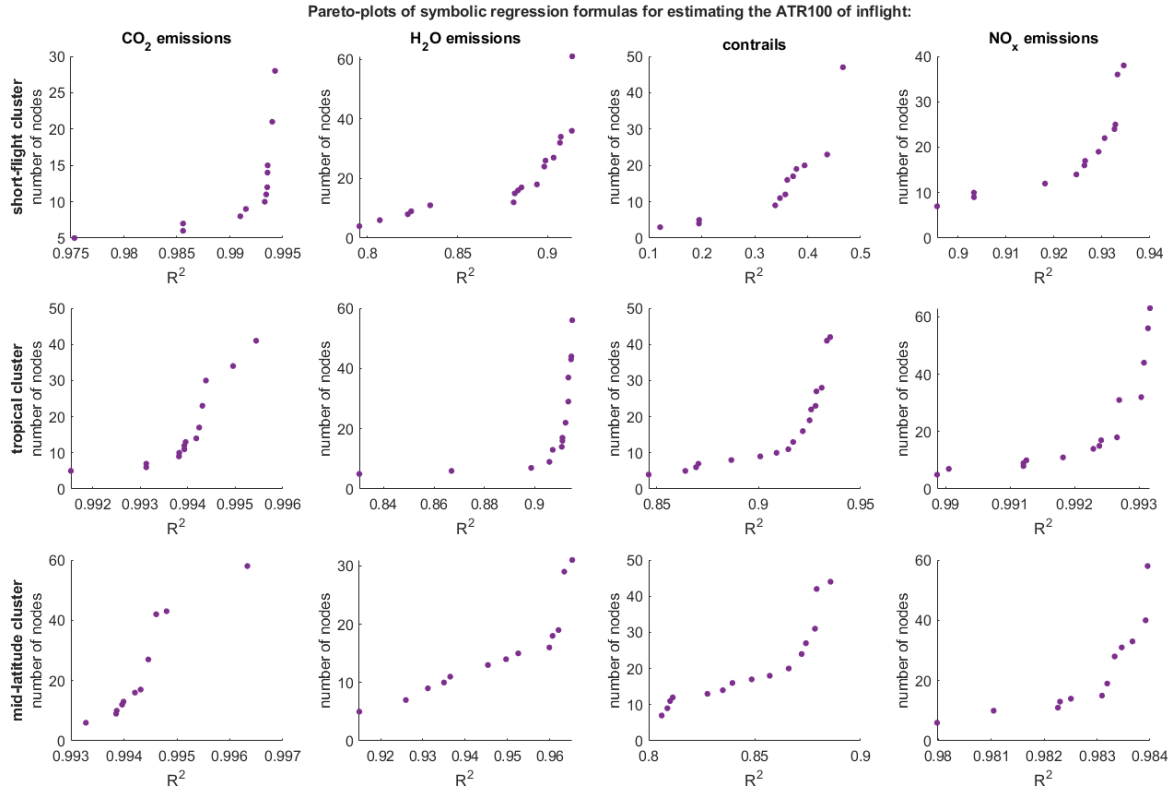


Figure S10. Pareto plots for the derived climate effect formulas from the clustered gridsearch for CO₂ and non-CO₂ effects.

170 R^2 as well as the root mean square error, used as the fitness function for the regression, are based on the sum of absolute errors for the whole dataset. This raises the challenge, that big relative errors might be underrepresented, if they are comparably small in absolute measures. In the context of the climate effect of flights, this means, that for flights with a small absolute climate

effect in the dataset, e.g. short flights, the formula-based estimation is less accurate, than for flights with a high absolute climate effect, e.g. long flights.

175 To combine the SR-formulas for the single species into a single formula for the total climate effect the formulas for CO₂, H₂O, CiC and NO_x have to be added (see Eq. 1; main article). Combining the formulas involves adding the number of nodes and recalculating R^2 . To identify the optimal formula for the total climate effect all combinations have to be tested, yielding one Pareto-plot of the combinations of all species for the unclustered version (marked blue in Fig. 4; main article) and three for the clustered version (purple), one per cluster (Fig. S11).

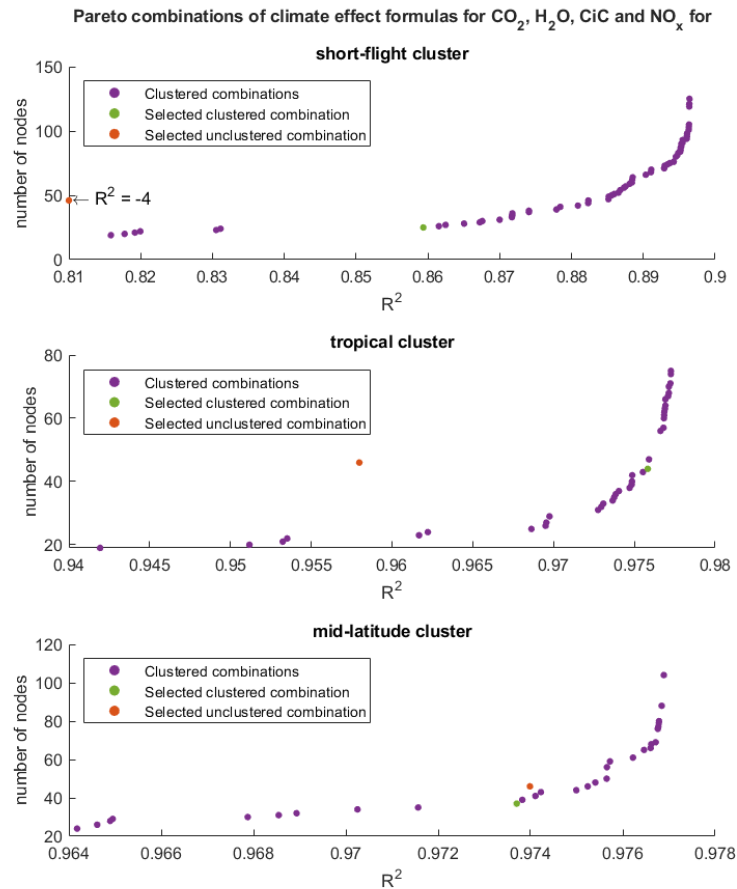


Figure S11. Pareto combinations of the clustered formulas for the total climate effect.

180 From the unclustered Pareto-combinations in Figure 4 (main article) the red one is selected because of its ratio of R^2 and mean node-count in a central position in the Parto-curve. For the clustered approach one Pareto combination is chosen per cluster. This is done by again combining the Pareto combinations from the plots in Figure S11. For every combination the resulting R^2 has to be newly computed and the node-counts have to be joined. From many potential options, the node-count

is calculated as the mean of the node-counts from the three clusters. From the resulting combinations the Pareto-individuals in terms of R^2 and mean node-count are determined.

Almost all Pareto-individuals do include the lowest- R^2 combination for the short-flight cluster from Figure S11, due to the under-representation of short-flights with low absolute climate effect in the R^2 -metric. Therefore the green marked combination in Figure S11 in the short-flight plot is manually selected for the short-flight cluster. The reason for this choice is, that the gain in R^2 compared to individuals with a lower node-count is far bigger, than the achievable gain for formulas with higher node-counts. This makes the Pareto individual a „sweet spot“. With this limitation the resulting Pareto-plot for the combination of all clusters is displayed in Figure 4 (main article) in purple. The selected green marked option for the clustered combinations in this plot is chosen similar to the unclustered one based on its ratio of R^2 and mean node-count. The corresponding individuals for the single clusters are marked green in Figure S11.

The selected unclustered formulas for CO₂ and non-CO₂ effects are displayed in the following.

$$\text{ATR100}_{\text{CO}_2, \text{unclustered}} = 3.8647 \times 10^{-8} + 6.8017 \times 10^{-11} \times d + 7.5994 \times 10^{-13} \times 0.0026 \times d \times (m + |\bar{\phi}|) \quad (\text{Eq. S20})$$

$$\text{ATR100}_{\text{H}_2\text{O}, \text{unclustered}} = 1.9098 \times 10^{-26} + 1.3696 \times 10^{-16} \times \frac{|\bar{\phi}| \times d \times m}{\log(d)} \quad (\text{Eq. S21})$$

$$\begin{aligned} \text{ATR100}_{\text{CiC}, \text{unclustered}} = & \max \left(0, -2.8964 \times 10^{-8} + 4.3954 \times 10^{-13} \times \left(\frac{\bar{\phi}^2}{-4.5238 \times 8.4089} \right)^2 \times d \right. \\ & \left. + 2.8962 \times 10^{-10} \times \arctan(e^{|\bar{\phi}|}) \times d \times \left(\frac{|\bar{\phi}|}{-4.5238} + \log(d) \right) \right) \end{aligned} \quad (\text{Eq. S22})$$

$$\text{ATR100}_{\text{NO}_x, \text{unclustered}} = 3.0437 \times 10^{-8} + 4.3928 \times 10^{-14} \times \frac{d \times m}{9.7573} \quad (\text{Eq. S23})$$

The selected clustered formulas are provided below. For the short-flight cluster:

$$\text{ATR100}_{\text{CO}_2, \text{short}} = 3.6007 \times 10^{-8} + 2.9714 \times 10^{-15} \times d \times (m + d) \quad (\text{Eq. S24})$$

$$\text{ATR100}_{\text{H}_2\text{O}, \text{short}} = \max(0, -7.2901 \times 10^{-10} + 2.3532 \times 10^{-14} \times \sqrt{m} \times d) \quad (\text{Eq. S25})$$

$$\text{ATR100}_{\text{CiC}, \text{short}} = \max \left(0, -3.4621 \times 10^{-8} + 2.3728 \times 10^{-10} \times \left(d - \frac{|\bar{\phi}|}{0.2806} \right) + 1.4310 \times 10^{-11} \times e^{\frac{|\bar{\phi}|}{6.8853}} \right) \quad (\text{Eq. S26})$$

$$\text{ATR100}_{\text{NO}_x, \text{short}} = 6.7429 \times 10^{-26} + 8.7635 \times 10^{-17} \times \frac{d^2 \times m}{\log(m)} \quad (\text{Eq. S27})$$

For the tropical cluster:

$$\text{ATR100}_{\text{CO}_2, \text{tropical}} = 8.2946 \times 10^{-8} + 2.7596 \times 10^{-14} \times \frac{d \times m}{\log(m)} \quad (\text{Eq. S28})$$

$$\text{ATR100}_{\text{H}_2\text{O}, \text{tropical}} = \max(0, -1.4086 \times 10^{-8} + 1.2768 \times 10^{-13} \times d \times \sqrt{m}) \quad (\text{Eq. S29})$$

$$\begin{aligned} \text{ATR100}_{\text{CiC}, \text{tropical}} = & \max \left(0, -1.6874 \times 10^{-6} - 2.4767 \times 10^{-10} \times \bar{\phi}^2 \times \sqrt{d} \right. \\ & \left. + 4.7552 \times 10^{-9} \times \left(\left(d + \sqrt{d} + (0.8622 \times \bar{\phi}^2) \right) + \frac{7.5484}{m} \times (\bar{\phi}^2 - d) \times d \right) \right) \end{aligned} \quad (\text{Eq. S30})$$

$$\text{ATR100}_{\text{NO}_x, \text{tropical}} = 3.0243 \times 10^{-24} + 4.6551 \times 10^{-15} \times d \times (d + m) \quad (\text{Eq. S31})$$

For the mid-latitude cluster:

$$\text{ATR100}_{\text{CO}_2, \text{mid-latitude}} = 8.1047 \times 10^{-8} + 2.7692 \times 10^{-14} \times \frac{d \times m}{\log(m)} \quad (\text{Eq. S32})$$

$$\text{ATR100}_{\text{H}_2\text{O}, \text{mid-latitude}} = 6.9866 \times 10^{-23} + 8.1065 \times 10^{-15} \times d \times \sqrt{m} \times |\bar{\phi}| \quad (\text{Eq. S33})$$

$$\text{ATR100}_{\text{CiC}, \text{mid-latitude}} = 1.1458 \times 10^{-20} + 2.7559 \times 10^{-13} \times \sqrt{m} \times \left(\frac{d}{\bar{\phi}}\right)^2 + 2.0812 \times 10^{-20} \times |\bar{\phi}|^5 \times d \times \sqrt{d} \quad (\text{Eq. S34})$$

$$215 \quad \text{ATR100}_{\text{NO}_x, \text{mid-latitude}} = 9.3398 \times 10^{-9} + 5.5456 \times 10^{-14} \times \frac{d \times m}{\log(m)} \quad (\text{Eq. S35})$$

In Figure 4 (main article) the unclustered Pareto-curve is about 0.01 to 0.02 lower in R^2 than the displayed clustered one. The selected clustered formula has a by 0.01 higher R^2 and 11 nodes less. In Figure S11 the performance of the selected unclustered formula for the single clusters is marked in red. Due to the described difficulties concerning the absolute and relative error, in particular the optimization for the absolute error metric R^2 , the unclustered formula is not suited to estimate the climate effect of flights of the short-flight cluster as it even has a negative R^2 for this part of the dataset. For the mid-latitude and the tropical cluster the unclustered formulas show a performance comparable to the clustered formulas with a high R^2 . In general the clustered formulas are better fitted to the conditions of the single clusters and thereby show a better overall performance in Figure 4 (main article).

This does also reflect in the MARE of the selected unclustered and clustered combinations of 51.7% and 29.0% over the whole dataset. MARE is defined according to Eq. 5 (main article) with N as the number of flights. Figure S12 shows, that the big difference between the two approaches is mainly caused by short flights. Due to the described difficulty caused by the absolute error used in R^2 , short flights are underrepresented in the optimization. This leads to estimates with high relative errors for those flights in the unclustered approach. As the clustered approach has a short-flight cluster, that separates short flights from longer ones, the relative error of the estimation for short flights is far lower.

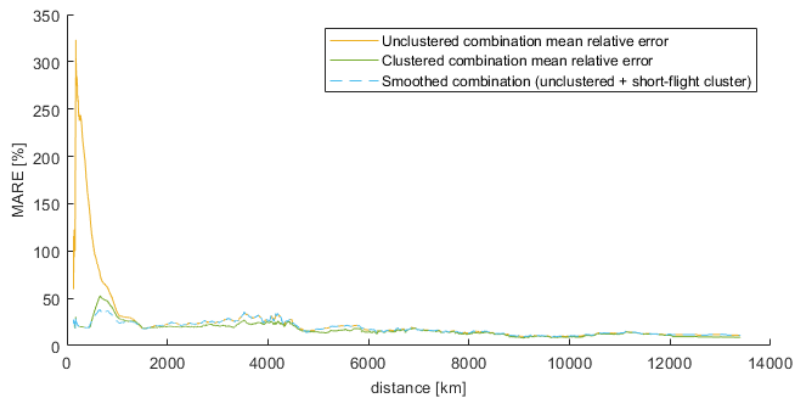


Figure S12. Comparison of the MARE for the unclustered and unclustered combinations, as well as the smoothed combination over the flight distance.

The recommend version of the SR-formulas is the combination of the short-flight cluster formulas for flights below 462.5 km flight distance and the unclustered formulas for all longer flights. So in this version there is only one cluster boundary at a distance of 462.5 km. The estimates of the unclustered formulas and the short-flight cluster formulas differ at the cluster boundary (see e.g. Fig. S13). The largest difference occurs for flights with light regional aircraft around the equator. In general the gap between the estimates is lowest in the mid-latitudes and increases around the poles and the equator. For heavier aircraft the difference between both estimates is lower than for light ones. The median of the difference over the whole field of application is about 30 % to 40 %. By smoothing the estimate around the cluster boundary misleading estimates and misincentives can be avoided. The R^2 -optimal smoothing boundary values are presented in Table S7.

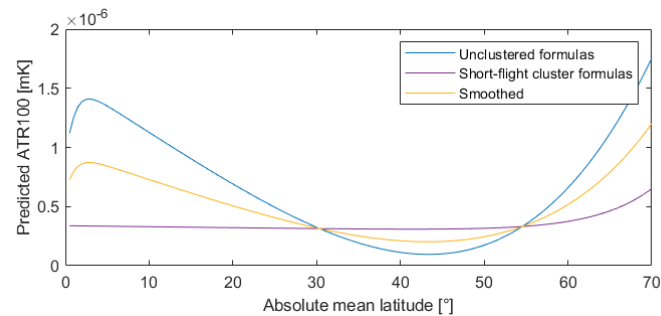


Figure S13. Difference in climate effect estimates at the cluster boundary of 462.5 km between the short-flight cluster formulas and the unclustered formulas, as well as the smoothed result for the A320-231.

Table S7. Definitions for smoothing of Symbolic Regression formulas

| Cluster boundary | Boundary value | Smoothing boundary 1 (b_{C1}) | Smoothing boundary 2 (b_{C2}) |
|---------------------|----------------|-----------------------------------|-----------------------------------|
| short - unclustered | 462.5 km | 50 km | 994 km |

The resulting quality of the smoothed version in comparison to the selected unclustered and clustered formulas, as well as the unsmoothed combination of unclustered and short-flight cluster formulas is displayed in Table S8. The trend of MARE over the distance for the smoothed version combines the unclustered and clustered advantages and even surpasses the single versions (Fig. S12). Through the use of the short-flight cluster formulas the estimation quality for shorter flights is greatly improved compared to the unclustered formulas. Caused by the smoothing the short-flight cluster formulas are applied to flights longer than the cluster boundary. This results in a lower MARE for flights between 500 to 1000 km than the unsmoothed combination of unclustered and short-flight cluster formulas as well as the pure the clustered and unclusterd versions, as the actual values in many cases lay in between the two estimates (Fig. S12). This leads to the smoothed version having the lowest MARE of all four options in Table S8.

Table S8. R^2 and MARE of the selected unclustered and clustered versions, as well as the unsmoothed and smoothed combination of unclustered and short-flight formulas.

| | Unclustered | Clustered | Unclustered & short-flight | Smoothed unclustered & short-flight |
|-------|-------------|-----------|----------------------------|-------------------------------------|
| R^2 | 0.9678 | 0.9761 | 0.9681 | 0.9684 |
| MARE | 51.7 % | 29.0 % | 29.0 % | 25.8 % |

S4 Climate effect allocation per passenger

To estimate the climate effect per passenger (PAX), a method is developed to allocate the total climate effect of a flight per
250 passenger. This allocation is aircraft type specific and distinguishes between Economy, Premium Economy, Business and First
Class passengers, reflecting their different spatial demands within the cabin.

The chosen allocation metric is the ratio of seat pitch to seat abreast. This ratio is summed across all available seats inside
an aircraft of all flight classes i , taking class-specific seating configurations into account, to determine the characteristic Cabin
Seating Length (CSL) of the aircraft.

255
$$CSL = \sum_i \frac{n_{seats,i}}{seat\ abreast_i} \cdot seat\ pitch_i \quad \text{with } i = \{\text{Economy, Premium Economy, Business, First Class}\} \quad (\text{Eq. S36})$$

The used seat abreast is always based on the maximum cell diameter of the aircraft. CSL describes the total length inside an
hypothetic cylindrical aircraft cabin with a constant maximum diameter, that is filled with seats. The idea is, that its value
should be as independent as possible from the specific seating configuration of an aircraft but rather describe the potential
physical space. In contrast to a simple area-based approach (seat pitch \times seat width), CSL also accounts for class-dependent
260 variations such as unused spaces between seats and differing aisle widths, making it the preferred concept of allocation for
this study. Differences in galley space, lavatories as well as the assigned number of cabin crew and baggage allowances across
flight classes are not captured in this method, which is considered acceptable due to the complexity and large data requirements
of including them.

CSL serves as the basis for allocating the flight’s climate effect to individual passengers. The applied allocation of climate
265 effect per passenger of a selected flight class i is thereby defined as follows:

$$ATR100_{\text{per PAX},i} = ATR100_{\text{per flight}} \cdot \frac{seat\ pitch_i}{seat\ abreast_i} \cdot CSL^{-1} \quad (\text{Eq. S37})$$

For the allocation implementation inside the *FlightClim v1.0* Excel tool, a statistical analysis is conducted based on data
from the Cirium Fleets Analyzer for the year 2023 (Cirium, 2025). For each aircraft type, the median CSL is calculated over all
aircraft with valid seating configuration data. Typical values for seat abreast and pitch per flight class are identified accordingly.
270 The resulting median CSL and the typical seat abreast per class are saved in the aircraft database of the tool. The seat pitch is
seen as a seat category specific parameter and is averaged over all aircraft within the same seat category. These values are listed
in the assumptions sheet and range from 31 inches for a Economy seat on a regional aircraft with 20-50 seats to 80 inches for
a First Class seat on a long haul aircraft with 302-600 seats.

Table S9. Values and parameters for the uncertainty estimate. RF values are given in mW/m^2 and the individual factors r are all dimensionless. L21 and G21 is referring to Lee et al. (2021) and Grewe et al. (2021). l and h stand for low and high.

| Effect | RF_x^{L21} | RF_x^{G21} | r_x^{ref} | ERF_x^{L21} | $ERF_x^{L21}(l)$ | $ERF_x^{L21}(h)$ | $r_x^{L21}(l)$ | $r_x^{L21}(h)$ | $r_x^{tot}(l)$ | $r_x^{tot}(h)$ |
|------------------|--------------|--------------|-------------|---------------|------------------|------------------|----------------|----------------|----------------|----------------|
| CO ₂ | 25.0 | 25.0 | 1.00 | 34.3 | 28 | 40 | 0.82 | 1.17 | 0.81 | 1.16 |
| H ₂ O | 1.4 | 0.6 | 2.38 | 2.0 | 0.8 | 3.2 | 0.40 | 1.60 | 0.95 | 3.80 |
| O ₃ | 24.0 | 40.3 | 0.60 | 49.3 | 32 | 76 | 0.66 | 1.54 | 0.39 | 0.92 |
| CH ₄ | -11.4 | -10.8 | 1.06 | -21.2 | -40 | -15 | 1.89 | 0.71 | 1.99 | 0.75 |
| PMO | -5.7 | -3.1 | 1.83 | -10.6 | -20 | -7.4 | 1.89 | 0.70 | 3.46 | 1.28 |
| NO _x | 6.6 | 26.4 | 0.25 | 17.5 | 0.6 | 29 | 0.03 | 1.66 | 0.01 | 0.41 |
| CiC | 67.5 | 45.1 | 1.50 | 57.4 | 17 | 98 | 0.30 | 1.71 | 0.44 | 2.55 |
| Total | 95.2 | 97.2 | 0.98 | 100.9 | 55 | 145 | 0.55 | 1.44 | 0.53 | 1.41 |

S5 Atmospheric uncertainty estimate

In Sec. 5.2 of the main paper, we describe how we break down the uncertainties from the global analysis to the individual climatological flight routes. The first step is to identify the relative location of the overall AirClim results to the Lee et al. (2021) best estimate. This is given by the ratio $r_x^{ref} = \frac{RF_x^{L21}}{RF_{AirClim}^{G21}}$, where we compare the RF values for 2005 as given in Grewe et al. (2021) for AirClim with the respective values from Lee et al. (2021) in their Table 3. In a second step, we use the 90%-confidence interval of Lee et al. (2021) for the 2018 ERF in relative numbers $r_x^{L21}(l/h) = \frac{ERF_x^{L21}(low/high)}{ERF_x^{L21}}$. Those values are given in Table S9. With this approach we use the ATR100 values as estimated with AirClim and relate to the uncertainty estimate (confidence intervals) from Lee et al. in a way that the sum of all flights in a year are consistent with the uncertainty ranges of Lee et al. (2021).

The calculated RF values for 2005 CO₂ agree very well between AirClim and the reference data and the confidence interval is between -9% and +16%. For contrails (CiC) the RF based on AirClim is smaller than the reference, but the values are still well in the confidence interval between -56% and +155%. Water vapour RF estimates are lower than the reference. And the calculated confidence interval is between -5% and +280%. Note that the overall effects from water vapour are small (but can be significant for higher flying subsonic aircraft) and that the underlying General Circulation Model simulations are performed with a Lagrangian advection scheme that show a good representation of the water vapour distribution at tropopause levels (Stenke et al., 2008). The short-term ozone responses are considerably larger than those in the reference data. While the vertical sensitivity of the ozone RF agrees well with other models (see Fig A.6 in Dahlmann et al. (2016) and Matthes et al. (2021)), the mean RF value is slightly outside the reference data confidence interval (-61% to -8%) which leads to a larger total NO_x-RF than in the reference data. However, note that for the NO_x-RF some methodological issues are still discussed (Grewe et al., 2019).

S6 Comparison to the model from Dahlmann et al. (2023)

295 For the comparison of the developed MR and SR models to the formulas from Dahlmann et al. (2023) based on the regression dataset of this study a metric conversion is necessary. The emission scenario of Dahlmann et al. (2023) are constant emissions over 32 years (LT32) while this study uses increasing emissions over 100 years (Fa1). Both studies feature the same indicator (ATR) and time horizon (100 years). The applied conversion factors are given in table S10 and Equation Eq. S38 approximates the conversion factor f_{conv} for the aggregated NO_x climate effect of the flight i . The ATR100 values refer to the values in the regression dataset (Fa1).

Table S10. Conversion factors f_{conv} from ATR100 with increasing emissions over 100 years (Fa1) to constant emissions over 32 years (LT32)

| CO_2 | H_2O | CiC | O_3 | CH_4 | PMO |
|---------------|----------------------|------|--------------|---------------|------|
| 0.41 | 0.26 | 0.26 | 0.26 | 0.33 | 0.33 |

$$f_{conv,NOx} = \frac{f_{conv,O3} \cdot |ATR100_{O3,i}| + f_{conv,CH4} \cdot |ATR100_{CH4,i}| + f_{conv,PMO} \cdot |ATR100_{PMO,i}|}{|ATR100_{O3,i}| + |ATR100_{CH4,i}| + |ATR100_{PMO,i}|} \quad (\text{Eq. S38})$$

In Table S11 and Figure S14 the estimation quality of the MR, SR and Dahlmann et al. (2023) formulas is compared for all flights with an Airbus A330-200 in the regression dataset and in Table S12 and Figure S15 for all flights in the dataset. We use the Fa1 emission scenario for the comparison. As Dahlmann et al. (2023) only includes formulas for the ratio of a species' climate effect to the CO_2 climate effect the comparison takes place for this ratio. Therefore H_2O , Cont, NO_x and Total in Tables S11, S12 and Figures S14, S15 refers to the ratio of these species. The correlation of contrail climate effect and wingspan is added to the Dahlmann et al. (2023) model according to Section S1 to enable comparability.

Table S11 and Figure S14 show, that the Dahlmann et al. (2023) model estimates the climate effect of A330 flights with a comparable and even slightly better quality than the models of this study with the contrail climate effect as an exception. We identified differences in the simulated cruise altitude as a potential reason for the worse fit by comparing the climate effect of A330 flights of the same route present in both datasets. In addition we think that the a further reason is the spatial concentration of flights in the Dahlmann et al. (2023) study where the current dataset has a broader geographical distribution, leading to a better global estimation of the MR and SR formulas. When applying the models to all flights in the regression dataset, it becomes clear, that the Dahlmann et al. (2023) formulas are only fitted to the Airbus A330 aircraft and are less applicable to other aircraft categories, whereas the MR and SR models show a comparable performance over all aircraft categories, indicating a valid estimation (see Table S12 and Figure S15).

In general no valid estimation is possible with a commonly used constant factor for the CO_2 to non- CO_2 ratio. Such a factor of 3.77 for the whole regression dataset leads to a RMSE of 2.6440, a MARE of 59 % and by definition a R^2 of 0.

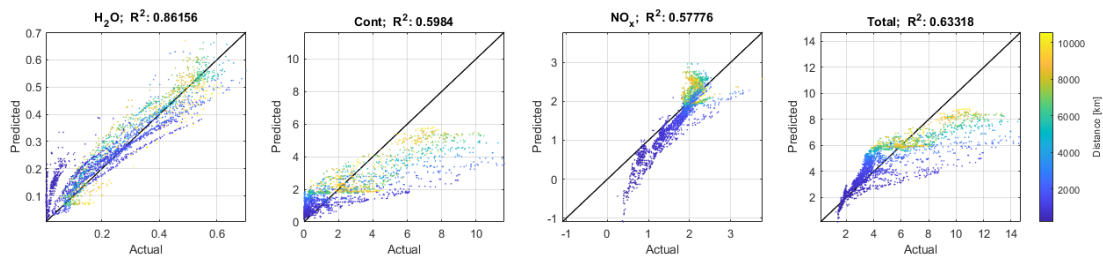
Table S11. Estimation quality of MR, SR and Dahlmann et al. (2023) (DL) formulas in terms of root mean squared error (RMSE), coefficient of determination (R^2), mean absolute relative error (MARE) for all Airbus A330-200 flights in the regression dataset.

| Regression formulas | | RMSE | R^2 | MARE |
|---------------------|-----|---------|--------|--------|
| H ₂ O: | DL: | 0.0642 | 0.8616 | - |
| | MR: | 0.0897 | 0.7303 | - |
| | SR: | 0.09233 | 0.6902 | - |
| NO _x : | DL: | 0.3393 | 0.5778 | 20.7 % |
| | MR: | 0.3856 | 0.4547 | 16.8 % |
| | SR: | 0.3533 | 0.5422 | 20.8 % |
| CiC: | DL: | 1.6314 | 0.5984 | - |
| | MR: | 0.9171 | 0.8731 | - |
| | SR: | 1.2486 | 0.7648 | - |
| Total: | DL: | 1.6920 | 0.6332 | 20.8 % |
| | MR: | 1.0619 | 0.8555 | 13.2 % |
| | SR: | 1.2907 | 0.7865 | 18.2 % |

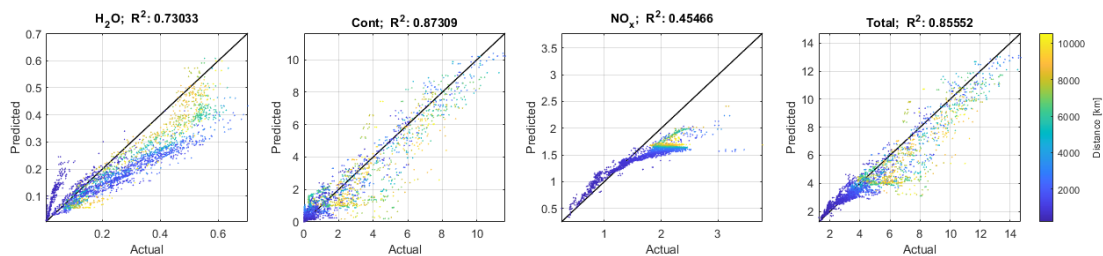
Table S12. Estimation quality of MR, SR and Dahlmann et al. (2023) (DL) formulas in terms of root mean squared error (RMSE), coefficient of determination (R^2), mean absolute relative error (MARE) for all flights in the regression dataset.

| Regression formulas | | RMSE | R^2 | MARE |
|---------------------|-----|--------|--------|--------|
| H ₂ O: | DL: | 0.1109 | 0.1898 | - |
| | MR: | 0.0800 | 0.5778 | - |
| | SR: | 0.0601 | 0.7620 | - |
| NO _x : | DL: | 0.5124 | 0.0951 | 84.9 % |
| | MR: | 0.2044 | 0.8560 | 18.5 % |
| | SR: | 0.2678 | 0.7529 | 24.1 % |
| CiC: | DL: | 2.2030 | 0.1657 | - |
| | MR: | 1.4406 | 0.6433 | - |
| | SR: | 1.3692 | 0.6777 | - |
| Total: | DL: | 2.2806 | 0.2560 | 31.6 % |
| | MR: | 1.4525 | 0.6982 | 21.8 % |
| | SR: | 1.3892 | 0.7239 | 25.9 % |

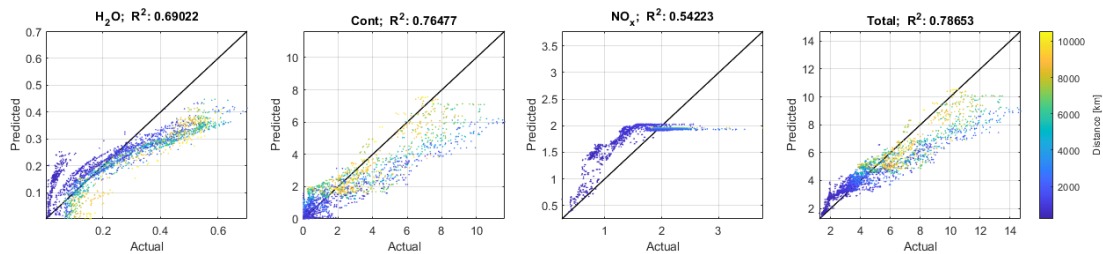
Figure S14. Comparison of the estimation quality MR, SR and Dahlmann et al. (2023) (DL) formulas for all Airbus A330-200 flights in the regression dataset. Actual refers to the value according to the regression dataset and Predicted is the estimation of the model for the ratio of the species' climate effect to the climate effect of CO₂.



(a) DL

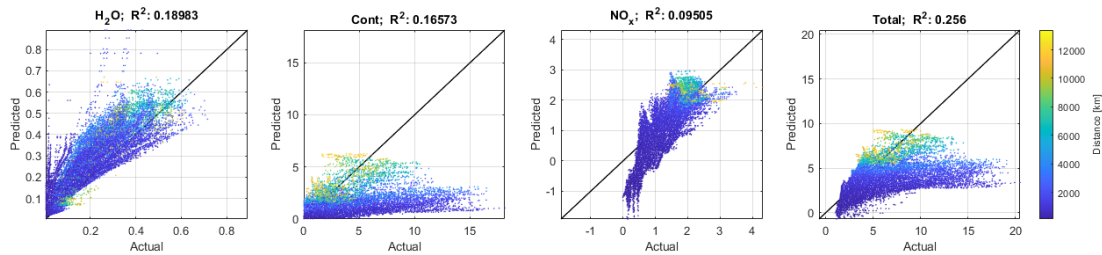


(b) MR

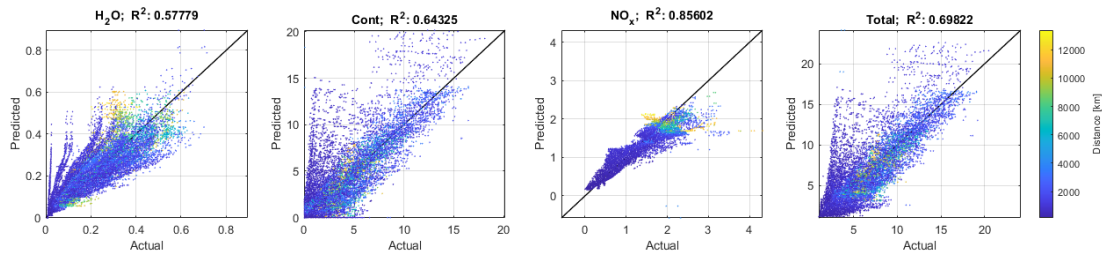


(c) SR

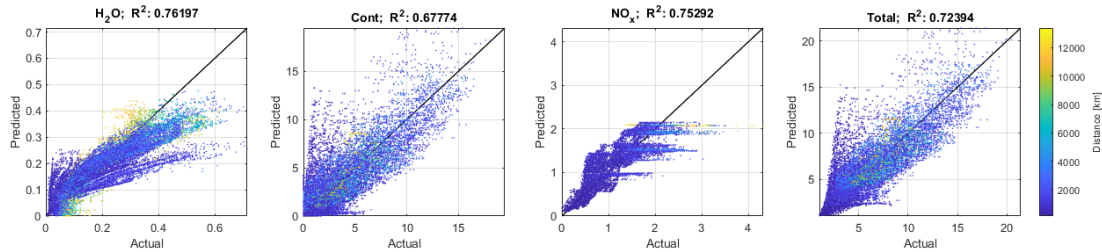
Figure S15. Comparison of the estimation quality MR, SR and Dahlmann et al. (2023) (DL) formulas for all flights in the regression dataset. Actual refers to the value according to the regression dataset and Predicted is the estimation of the model for the ratio of the species ´ climate effect to the climate effect of CO₂.



(a) DL



(b) MR



(c) SR

320 S7 User guide

For simplifying the estimation of CO₂ equivalents per flight, the resulting regression formulas of the MR-approach for the climate effect, fuel and NO_x are embedded into the Excel application *FlightClim v1.0*. The basic user version of the Excel application consists of the three main Excel sheets: “Info”, “CO₂e Calculator”, and “Checks”:

1. The “Info” sheet provides general information such as the release date and the version number. In addition, you will find an instruction for the use of *FlightClim* and an exclusion of liability.

2. The “CO₂e Calculator” sheet is the core of *FlightClim*. All input values are entered in this sheet and all calculation results are displayed.

3. The "Checks" sheet includes consistency checks of the input and thereby helps to find errors in the input parameters.

330 Hidden there are eight more Excel sheets implementing the internal functionality of *FlightClim*: "Assumptions", "Climate metrics", "Per PAX Share", "Multiple Regressions", "GC Calculator", "Airport Database", "Aircraft Database", "Regression coefficients":

1. The "Assumptions" sheet includes the main assumptions of *FlightClim*. This includes the conversion factors for the included climate metrics as well as the different seat categories with their reference aircraft and assumed seat pitches for all flight classes.

335 2. The "Climate metrics" sheet covers the conversion from the ATR100 metric with increasing emissions to all other available climate metrics. Available climate metrics are ATR100 (Pulse Emissions), ATR100 (Increasing Emissions), EAGWP100 (Pulse Emissions), EAGWP100 (Increasing Emissions), AGWP100 (Increasing Emissions). The AGWP is the Absolute Global Warming Potential and EAGWP stands for the Efficacy Weighted Absolute Global Warming Potential, that is used for the Monitoring, Reporting and Validation scheme of the European Union.

340 3. The "Per PAX Share" sheet estimates the share a passenger has on the climate effect of the total flight according to the procedure described in section S4 of this Supplementary Material.

4. The "Multiple Regressions" sheet implements the MR-formulas as well as the Fuel- and NO_x-functions.

5. The "GC Calculator" sheet includes the calculation of the great circle distance between the origin and destination airports as well as the mean great circle latitude. Both parameters are required as input for the regression formulas. To account
345 for the common deviation from the most direct great circle route 95 km are added to the great circle distance for every flight.

6. The "Airport Database" sheet provides detailed position information for almost 9000 airports. Airports are identified via the IATA airport code, which is a three-letter geocode defined by the International Air Transport Association (IATA).

7. The "Aircraft Database" sheet includes characteristics of 65 common jet aircraft types used in the spanwise adaption of the CiC climate effect and the per PAX allocation. Each aircraft is identified by its ICAO Aircraft Type Designator, that
350 is a four-letter code issued by the International Civil Aviation Organization (ICAO).

8. The "Regression coefficients" sheet provides the coefficients for the MR-formulas, as well as the Fuel- and NO_x-functions.

The calculations of the climate impact expressed in CO_{2,e} is based on the following input parameters, which users enter into
355 the “CO₂e Calculator” sheet of *FlightClim*:

1. Selection of the Aircraft Identifier input type in cell "A2". The drop-down list allows the user to choose between the ICAO Aircraft Type Designator and the Seat Category.
2. Selection of the preferred climate metric from a drop-down list for the calculation of CO_{2,e} in cell "B2".
3. Selection of the Aircraft Identifier in column "A". A drop-down list allows the user to choose between seven different seat categories and 65 ICAO Aircraft Type Designator. The proposed seat categories range from 101-151 seats to 302-600 seats and represent the following example aircraft types with the selected reference aircraft underlined:
 - 20-50 seats: like Bombarier CRJ200, Embraer ERJ-135/140/145
 - 51-100 seats: like Bombardier CRJ700/900, Embraer ERJ-170/175/190/195, Fokker 70/100
 - 101-151 seats: like Airbus A319, A320, Boeing 737
 - 152-201 seats: like Airbus A320, A321, Boeing 737, 757
 - 202-251 seats: like Airbus A330, A340, Boeing 767, 777
 - 252-301 seats: like Airbus A330, Boeing 777
 - 302-600 seats: like Airbus A340, A380, Boeing 747, 777
4. Input of the IATA airport code of the origin and destination airports in columns "B" and "C".
5. The number of flights performed on the city pair connection is entered into column "D". The value "1" is the minimum input value here.
6. Selection of a flight class for the estimation of per PAX CO_{2,e} from a drop-down list in column "E". Available flight classes are "First", "Business", "Premium Economy", "Economy".
7. Column "F" indicates whether all required inputs have been made and are valid. If "no" is indicated the "Checks" sheet helps to see which of the entries is not given or invalid.
8. Column "G" indicated whether the chosen flight class is available in the given aircraft.

If all entries have been made correctly, *FlightClim* will return the following output data in columns "H" to "U" of the "CO_{2e} Calculator" sheet:

- Column "H" gives the calculated great circle distance plus 95 km for arrival and departure procedures (in km),
- Column "I" provides the fuel burn estimate (in kg),
- Column "J" shows the CO₂ emissions resulting from the fuel burn with a linear factor of 3.16 (in kg),
- Column "K" gives the estimated CO₂ equivalent emissions of all non-CO₂ effects (in kg),

- Column "L" shows the estimated CO₂ equivalent emissions of all effects (CO₂ + non-CO₂) (in kg)
- Column "M" provides the estimated ration between total CO_{2,e} and CO₂ (CO_{2,e} factor),
- 385 – Columns "N" to P gives the CO₂ emission, CO_{2,e} emissions of all non-CO₂ effects and total CO_{2,e} emission per PAX,
- Column "Q" gives the seat load factor,
- Column "R" gives the share of 1 PAX to the total climate effect of the chosen flight for the selected flight class,
- Columns "S" to U give the estimated CO_{2,e} emission individually for water vapor (H₂O, column "S"), nitrogen oxides (NO_x, column "T") and contrail induced cloudiness (CiC, column "U").
- 390 In row 2 of the *FlightClim* “CO₂e Calculator” sheet, aggregated values are displayed for the distance, fuel consumption, CO₂ emissions, and CO_{2,e} (total value, value of all non-CO₂ effects, mean factor).

References

- Cirium: Fleets Analyzer 2023, <https://www.cirium.com/analytics-services/fleets-analyzer>, accessed: 2025-06-26, 2025.
- 395 Dahlmann, K., Grewe, V., Frömming, C., and Burkhardt, U.: Can we reliably assess climate mitigation options for air traffic scenarios despite large uncertainties in atmospheric processes?, *Transportation Research Part D: Transport and Environment*, 46, 40–55, <https://doi.org/10.1016/j.trd.2016.03.006>, 2016.
- Dahlmann, K., Grewe, V., Matthes, S., and Yamashita, H.: Climate assessment of single flights: Deduction of route specific equivalent CO₂ emissions, *International Journal of Sustainable Transportation*, 17, 29–40, <https://doi.org/10.1080/15568318.2021.1979136>, 2023.
- Grewe, V., Matthes, S., and Dahlmann, K.: The contribution of aviation NO_x emissions to climate change: are we ignoring methodological
400 flaws?, *Environmental Research Letters*, 14, 121 003, <https://doi.org/10.1088/1748-9326/ab5dd7>, 2019.
- Grewe, V., Gangoli Rao, A., Grönstedt, T., Xisto, C., Linke, F., Melkert, J., Middel, J., Ohlenforst, B., Blakey, S., Christie, S., Matthes, S., and Dahlmann, K.: Evaluating the climate impact of aviation emission scenarios towards the Paris agreement including COVID-19 effects, *Nature Communications*, 12, 3841, <https://doi.org/10.1038/s41467-021-24091-y>, 2021.
- Köhler, M., Rädcl, G., Shine, K., Rogers, H., and Pyle, J.: Latitudinal variation of the effect of aviation NO_x emissions on atmospheric ozone
405 and methane and related climate metrics, *Atmospheric Environment*, 64, 1–9, <https://doi.org/10.1016/j.atmosenv.2012.09.013>, 2013.
- Lee, D., Fahey, D., Skowron, A., Allen, M., Burkhardt, U., Chen, Q., Doherty, S., Freeman, S., Forster, P., Fuglestedt, J., Gettelman, A., De León, R., Lim, L., Lund, M., Millar, R., Owen, B., Penner, J., Pitari, G., Prather, M., Sausen, R., and Wilcox, L.: The contribution of global aviation to anthropogenic climate forcing for 2000 to 2018, *Atmospheric Environment*, 244, 117 834, <https://doi.org/10.1016/j.atmosenv.2020.117834>, 2021.
- 410 Matthes, S., Lim, L., Burkhardt, U., Dahlmann, K., Dietmüller, S., Grewe, V., Haslerud, A. S., Hendricks, J., Owen, B., Pitari, G., Righi, M., and Skowron, A.: Mitigation of non-CO₂ aviation’s climate impact by changing cruise altitudes, *Aerospace*, 8, 36, <https://doi.org/10.3390/aerospace8020036>, 2021.
- Searson, D. P.: GPTIPS 2: An Open-Source Software Platform for Symbolic Data Mining, in: *Handbook of Genetic Programming Applications*, edited by Gandomi, A. H., Alavi, A. H., and Ryan, C., pp. 551–573, Springer International Publishing, Cham,
415 https://doi.org/10.1007/978-3-319-20883-1_22, 2015.
- Stenke, A., Grewe, V., and Ponater, M.: Lagrangian transport of water vapor and cloud water in the ECHAM4 GCM and its impact on the cold bias, *Climate Dynamics*, 31, 491–506, <https://doi.org/10.1007/s00382-007-0347-5>, 2008.
- Unterstrasser, S.: The Contrail Mitigation Potential of Aircraft Formation Flight Derived from High-Resolution Simulations, *Aerospace*, 7, 170, <https://doi.org/10.3390/aerospace7120170>, 2020.
- 420 Unterstrasser, S. and Görsch, N.: Aircraft-type dependency of contrail evolution, *J. Geophys. Res. Atmos.*, 119, 14 015–14 027, <https://doi.org/10.1002/2014JD022642>, 2014.